nature materials

LETTERS

https://doi.org/10.1038/s41563-019-0482-5

Ultralow-threshold, continuous-wave upconverting lasing from subwavelength plasmons

Angel Fernandez-Bravo[1,7], Danqing Wang[2,7], Edward S. Barnard[1], Ayelet Teitelboim[1], Cheryl Tajon[1,3], Jun Guan[2], George C. Schatz[2,4], Bruce E. Cohen[1], Emory M. Chan[1], P. James Schuck[1,5*] and Teri W. Odom[2,4,6*]

Miniaturized lasers are an emerging platform for generating coherent light for quantum photonics, in vivo cellular imaging, solid-state lighting and fast three-dimensional sensing in smartphones[1–3]. Continuous-wave lasing at room temperature is critical for integration with opto-electronic devices and optimal modulation of optical interactions[4,5]. Plasmonic nanocavities integrated with gain can generate coherent light at subwavelength scales[6–9], beyond the diffraction limit that constrains mode volumes in dielectric cavities such as semiconducting nanowires[10,11]. However, insufficient gain with respect to losses and thermal instabilities in nanocavities has limited all nanoscale lasers to pulsed pump sources and/or low-temperature operation[6–9,12–15]. Here, we show continuous-wave upconverting lasing at room temperature with record-low thresholds and high photostability from subwavelength plasmons. We achieve selective, single-mode lasing from Yb^{3+}/Er^{3+}-co-doped upconverting nanoparticles conformally coated on Ag nanopillar arrays that support a single, sharp lattice plasmon cavity mode and greater than wavelength $\lambda/20$ field confinement in the vertical dimension. The intense electromagnetic near-fields localized in the vicinity of the nanopillars result in a threshold of 70 W cm^{-2}, orders of magnitude lower than other small lasers. Our plasmon-nanoarray upconverting lasers provide directional, ultra-stable output at visible frequencies under near-infrared pumping, even after six hours of constant operation, which offers prospects in previously unrealizable applications of coherent nanoscale light.

Lanthanide-based upconverting nanoparticles (UCNPs) are photostable solid-state non-linear emitters that are efficient at sequentially absorbing multiple near-infrared (NIR) photons and emitting at visible and shorter-NIR wavelengths[16–19]. Recently, UCNPs have been used as gain media in small lasers, and their integration with dielectric microcavities and hyperbolic metamaterials has resulted in multi-wavelength upconverted lasing[20–22]. UCNPs also exhibit long radiative lifetimes (typically 100 s of μs) compared to other gain materials[18,23,24], which leads to low saturation intensities that could facilitate continuous (CW) pumping and population inversion build-up. Pump powers required for UCNP lasing are orders of magnitude lower than those for nanolasers based on quantum dots, dye molecules or conventional non-linear optical materials[7,22,25]. Additionally, organic molecules exhibit triplet-state accumulation and limited photostability, and semiconductor nanomaterials undergo Auger recombination, which reduces population inversion under CW pump[4,26,27].

Multiphoton upconverting processes can be strongly enhanced by the intense electromagnetic fields from plasmonic nanostructures[28]. However, surface plasmon resonances from single nanoparticles are typically broadband with low mode quality. Spectral overlap with multiple, narrow UCNP energy bands results in reduced output efficiency at a single targeted mode because of internal energy transfer[29,30]. Arrays of metal nanoparticles can overcome these challenges because collective, coherent coupling can produce narrow lattice plasmon resonances (linewidths <5 nm) with suppressed radiative loss and stronger near-field enhancements compared to single nanoparticles[31,32]. Previously, we demonstrated band-edge lattice plasmons as optical feedback for down-shifted dye nanolasing at room temperature with directional emission and tuneable wavelengths[6,7,33,34]. Compared to photonic microcavities that exhibit multiple cavity modes[21], plasmonic nanocavity arrays with a single lattice spacing support a single, narrow mode that can, in principle, selectively enhance specific upconverting energy transitions.

We designed plasmon lasers that integrate two key advances to enhance coupling between the nanocavity and the lanthanide ion (Ln^{3+}) emitters, to lower upconverting lasing thresholds and to improve device stability. First, we fabricated Ag nanopillar arrays with a lattice plasmon resonance that overlaps the red Er^{3+} upconverted emission transition ($^4F_{9/2}$ to $^4I_{15/2}$) in colloidal UCNPs doped with sensitizer Yb^{3+} ions/emitter Er^{3+} ions (Fig. 1a–c). Second, we exploited core–shell UCNPs with high Ln^{3+} content that are known to show improved luminescence properties and considerably reduced saturation intensities compared to canonical compositions[24,35–37]. The high-Ln^{3+}-content UCNPs are core–shell heterostructures with 13.9 ± 1.3 nm diameters comprising 9.9-nm β-phase $NaYF_4$ cores doped with 20% Yb^{3+}/20% Er^{3+} and 2-nm $NaYF_4$ shells (Methods and Supplementary Fig. 1)[38]. In our all-solid-state system under ambient conditions, NIR pumping at 980 nm can excite Yb^{3+} ions in the UCNPs, which transfer energy to Er^{3+} ions to facilitate upconverted emission at multiple visible and NIR wavelengths, and lattice plasmon modes can be engineered to couple selectively to Er^{3+} emission (red) (Fig. 1d).

[1]The Molecular Foundry, Lawrence Berkeley National Laboratory, Berkeley, CA, USA. [2]Graduate Program in Applied Physics, Northwestern University, Evanston, IL, USA. [3]Trilo Therapeutics, San Francisco, CA, USA. [4]Department of Chemistry, Northwestern University, Evanston, IL, USA. [5]Department of Mechanical Engineering, Columbia University, New York, NY, USA. [6]Department of Materials Science and Engineering, Northwestern University, Evanston, IL, USA. [7]These authors contributed equally: Angel Fernandez-Bravo, Danqing Wang. *e-mail: p.j.schuck@columbia.edu; todom@northwestern.edu

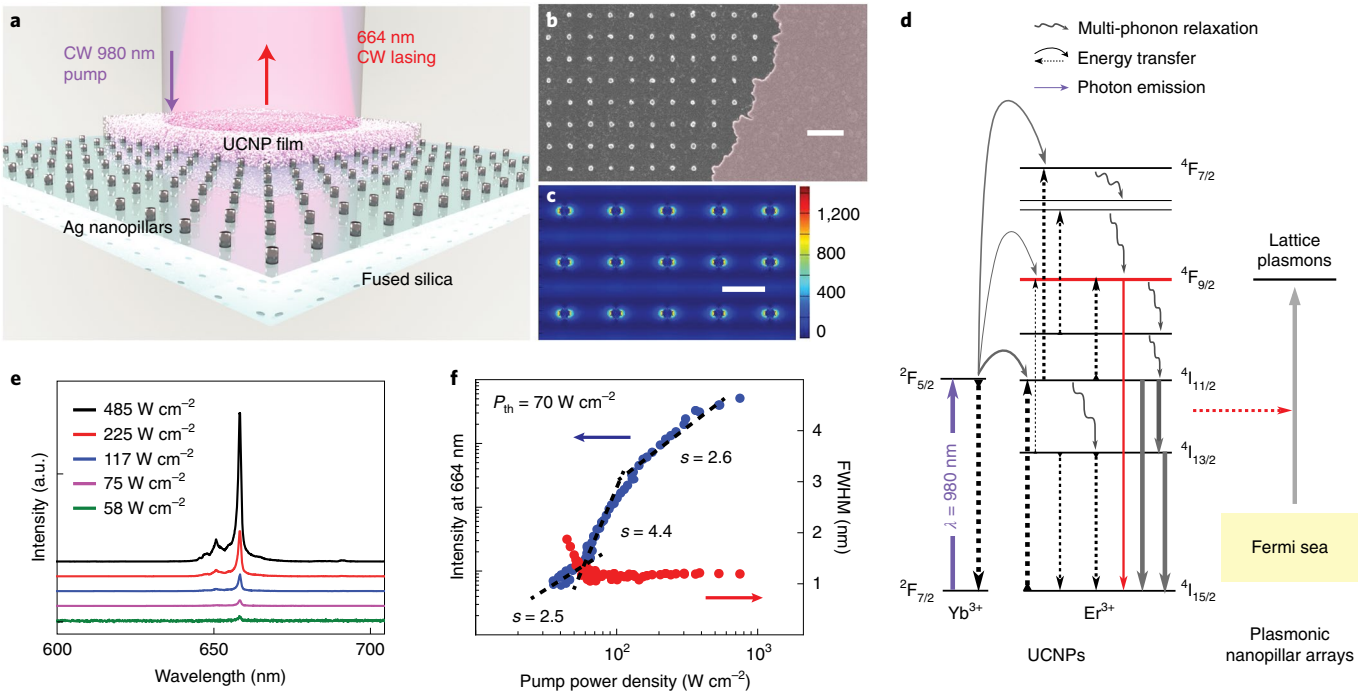

Fig. 1 | CW upconverting nanolasing on Ag nanopillar arrays at room temperature. a, Schematic of the UCNP coating on top of Ag arrays with spacing $a_0 = 450$ nm. Ag nanopillars are with 80-nm diameter, 50-nm height and the arrays are scalable over cm^2 areas. The UCNP film is roughly 150 nm thick. **b**, Scanning electron micrograph showing the Ag nanopillar array with partial conformal coating (right) with a film of 14 nm core–shell UCNPs ($NaYF_4$:Yb^{3+}, Er^{3+}). Scale bar, 1 μm. **c**, Representative near-field $|E|^2$ plot for the 450-nm spaced Ag nanopillars at resonance ($n = 1.46$) from a FDTD method simulation. Scale bar, 500 nm. **d**, Yb^{3+}, Er^{3+} energy levels and coupling mechanism to the lattice plasmons. **e**, Power-dependent lasing spectra from lattice plasmon resonances at $\lambda = 664$ nm for Ag nanopillar arrays with $a_0 = 450$ nm. Spectrometer resolution is 0.1 nm. **f**, Input–output curves in log–log scale with emission linewidth narrowing, showing a low lasing threshold P_{th} of 70 W cm^{-2}. FWHM, full width half maximum.

The plasmonic arrays consist of Ag nanopillars (80-nm diameter, 50-nm height) arranged in a square lattice with periodicity a_0 ranging from 450–460 nm depending on which transition within the Er^{3+} red emission manifold was of interest (Fig. 1a–c). As described previously[31,32], collective coupling of plasmonic nanopillar arrays produces a sharp lattice plasmon mode with a quality factor $Q = \frac{\lambda}{\Delta\lambda} > 200$ that is maintained after coating with UCNPs (Supplementary Fig. 2). UCNPs were drop-cast from solution onto the arrays to form conformal films of thickness around 150 nm, resulting in UCNPs that are situated at the nanoscale plasmonic hotspots within 25 nm surrounding each nanopillar surface (Fig. 1a–c; near-field enhancement at the nanopillars, electric field intensity $|E|^2/|E_0|^2 > 1{,}000$). Since the refractive index n of UCNPs ($n = \sim 1.47$ at 660 nm) closely matches that of the fused silica substrate ($n = \sim 1.46$ T 660 nm) (Supplementary Fig. 2), the Ag nanopillars were effectively embedded in a uniform index environment, which is critical for sustaining high-quality lattice plasmons.

To determine whether UCNPs are coupled to the plasmonic nanocavities, we first characterized spontaneous emission from UCNPs on the plasmonic array at low (around 20 W cm^{-2}) pump intensities. Enhanced upconverted emission between 650–660 nm was resolved at each Ag nanopillar position (Supplementary Fig. 3). As CW pump intensity increased beyond a threshold, lasing action occurred at the lattice plasmon resonance wavelength (Fig. 1e). At threshold, we observed both a significant increase in rising slope ($s = 4.4$) in the input–output curve compared to spontaneous emission ($s = 2.2$; Supplementary Fig. 4) and simultaneous linewidth narrowing of the lasing mode to <1 nm (Fig. 1f, Supplementary Fig. 5 and Supplementary Table 1). The measured linewidths above threshold are consistent with those observed in dye-based lattice plasmon lasers[6,7,33]. The lasing threshold of 70 W cm^{-2} from the device in Fig. 1 represents a >200-fold improvement over that of upconverting microresonators[21] and orders of magnitude reduction over that of nanodisk-on-film[12,39] or nanowire-on-film[14,15] plasmon lasers at room temperature (Supplementary Table 3). The low thresholds of our UCNP plasmon lasers (as low as 29 W cm^{-2}, Supplementary Fig. 6) can be attributed to both bright Yb^{3+}/Er^{3+}-co-doped UCNPs and single-mode plasmon nanocavities with spectrally selective optical enhancement. The measured external quantum efficiency of 0.04% is consistent with expectations based on Purcell enhancements and known upconverting quantum yield for these UCNPs (Supplementary Figs. 7 and 8).

Besides enabling low thresholds, plasmonic array nanocavities offer directional and highly efficient coupling, in contrast to spherical and cylindrical cavity geometries based on whispering gallery modes, where input coupling is non-trivial and emission is less directional. The collective coupling between periodic Ag nanopillars results in directional, beam-like upconverted emission at the band-edge Γ point[7] with a low divergence angle of around 0.5° (Fig. 2a,b). Additionally, the lasing beam is polarized along the same direction as the incident pump (Fig. 2c,d). This polarization coherence is distinct from unpolarized spontaneous emission from UCNPs (regardless of excitation polarization) that results from energy transfer migration between dopant ions within a single UCNP over the long lifetimes of Ln^{3+} excited states[23] and random nanocrystal orientation[40]. Moreover, our upconverting nanolaser shows long-term stability, which is typically challenging for multiphoton lasing systems since high peak pump intensities are often required for non-linear responses[21]. Our all-solid-state system operated at room temperature for more than 6 h under continuous irradiation, the longest operational period we tested (Fig. 2e,f). Over this time, we did not observe any optical or thermal damage; the

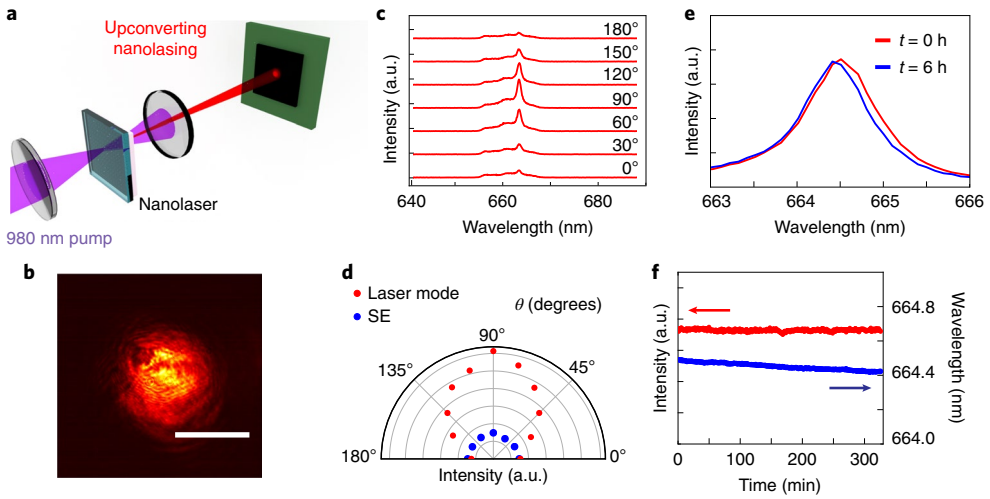

Fig. 2 | Upconverting nanolasing showed spatial and polarization coherence, as well as high photostability. a, Schematic of the experimental optics setup to measure the far-field beam profile. The excitation beam is filtered out using a short-pass 745 nm filter and 660/10 nm band pass filter, enabling the complementary metal-oxide-semiconductor sensor to record only the emission from the plasmon nanolasing at 664 nm. **b**, Far-field beam profile of lasing emission above threshold, with the camera detector placed 2 cm away from the sample plane, showing a beam divergence (the white bar) of around 0.5°. **c**, Polarization-dependent lasing emission with pump polarized at 90°. **d**, The polar plot represents the emission intensity of the 664 nm lasing mode and the spontaneous emission (SE) as a function of the polarization angle θ. **e**,**f**, Stability of lasing spectra, intensity and wavelength (red and blue curves) over the course of 6 h of uninterrupted irradiation, exhibiting stable emission intensity and modest mode shift (<0.15 nm).

mode intensity remained constant and only minimal shifts in mode frequency (<0.15 nm) occurred. In contrast, CW lasing based on semiconductor nanoparticles was not stable over 1 h under fluences similar to those used in this study[4,26].

We find that CW lasing occurs even under pulsed pumping conditions in our upconverting plasmon nanolaser (Fig. 3). This observation is consistent with excited state lifetimes that are much longer than both the pulse width and repetition period of the pulsed pump (~120 fs and ~13 ns, respectively). In contrast to measured spontaneous emission lifetimes of around 100 µs for these UCNPs[24], the lifetime curve for lasing emission at 660 nm within a 1-µs time window shows a bi-exponential fit with a slower component of 510 ns and a faster component of 66 ns (Supplementary Fig. 9 and Supplementary Table 2). These values agree well with our estimated range of Purcell enhancement factors (Supplementary Fig. 8), with increased decay rates for decreased Er^{3+}-nanopillar separation distances. Second-order correlation measurements ($g^{(2)}(\tau)$) of lasing emission confirm CW output (Supplementary Figs. 10–12). The lasing thresholds under pulsed pumps (in terms of average power) are similar to those under CW pumps (Supplementary Table 3).

To highlight the ability of the system to select specific Er^{3+} transitions for lasing, we varied the nanopillar lattice constant a_0, which modified the lattice plasmon nanocavity mode. Shifting the resonance from 650 nm (a_0 = 450 nm) to 660 nm (a_0 = 460 nm), we observed that the upconverted lasing emission followed the cavity mode resonance, demonstrating that single-mode upconverting lasing is directly determined by the plasmonic nanocavities (Fig. 3a). We found similar lasing thresholds and power dependencies for both lattice spacings, including high non-linearity in the gain portion of the input–output curves (s = 5.3 and 4.7 above the threshold for the devices with modes at 650 nm and 660 nm, respectively, Fig. 3b). Note that the extreme saturation of excited states under pulsed excitation led to a smaller rising slope (s = 1.2) at high pump powers.

To gain insight into the lasing mechanisms of these low-threshold upconverting nanolasers, we developed a semiquantum model and a time-domain approach to study the non-linear optical build-up under a pulsed pump (Fig. 3c). The narrow lattice plasmon resonance provides selective enhancement only for the $^4F_{9/2}$-to-$^4I_{15/2}$ red emission without directly affecting energy transfer processes at other energies. Therefore, we used a simplified six-level model to approximate the multiphoton optical pump process[19], different from the single-photon pump, four-level system[7] for dye-based plasmon nanolasers (Supplementary Fig. 13). The calculations show a large exponentially rising slope (s = 4.8) above the lasing threshold, which is similar to non-linear build-up seen in the experiments (Fig. 3d). In contrast, the slow rise close to threshold (s = 1.8) corresponds to the intrinsic two-photon emission of Yb^{3+}/Er^{3+}-co-doped UCNPs. To capture the time-dependent lasing build-up, we tracked the evolution of population density in different energy levels and found a characteristic population inversion from $^4F_{9/2}$ to $^4I_{15/2}$ above threshold (Fig. 3e). No population inversion was observed for upconverted emission below threshold, consistent with a slow rising slope (Supplementary Figs. 14 and 15). The calculated lasing threshold occurred at an average power of 270 W cm^{-2} (Fig. 3d), comparable with experiments. Minor differences in threshold are likely because of unknown gain values for the UCNPs and the simplified Er^{3+} electronic structure in our model, where we included only select Er^{3+} excited states.

In summary, we demonstrated CW upconverting plasmon nanolasing at room temperature. We observed exceptionally stable lasing over long periods (>6 h), with lasing thresholds as low as 29 W cm^{-2}, significantly lower than other plasmon and upconverting nanolasers. In addition, the upconverting nanolaser can achieve CW emission under both CW and pulsed pump conditions. Our time-domain, semiquantum modelling captured the characteristic population inversion and strong optical non-linearities. Low-threshold upconverting nanolasers with NIR pump open possibilities for integration with compact, low-power circuits as well as in vivo applications including deep-tissue imaging, sensing, theranostics and optogenetic manipulation[41]. Looking forward, the large variety of available output wavelengths in the Ln series, the ability to couple plasmonic nanocavities with densely packed quantum emitters and the general nanocavity architectures provide an almost unlimited number of robust low-power coherent nanoscale light sources. Our all-solid-state nanolaser platform offers prospects to realize quantum-optical technologies and commercial lab-on-a-chip photonic devices.

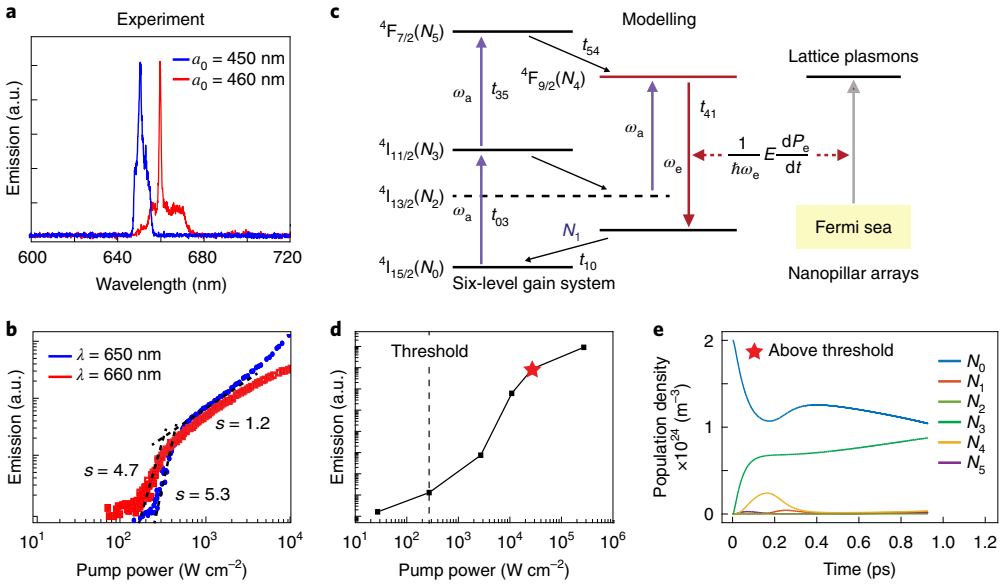

Fig. 3 | Upconverting CW nanolasing under a pulsed laser and semiquantum modelling in the time domain. a, Lasing spectra with lasing modes at $\lambda = 650$ and 660 nm from UCNPs coupled to Ag nanopillar arrays with spacing $a_0 = 450$ (blue) and 460 nm (red), respectively. The results show the selective coupling between Er^{3+} red emission from components of the $^4F_{9/2}$ level and the tailored plasmon resonances associated with collective Bragg modes of the Ag nanopillar arrays. **b**, Input–output curves in log–log scale show a slightly lower laser threshold for the mode at 660 nm. **c**, Six-level model system describing upconverting nanolasing and the associated population inversion. N denotes the population density, P_e is the net macroscopic polarization, and ω_a and ω_e are absorption and emission frequencies, respectively. The transition lifetimes are $t_{54} = t_{10} = 10$ fs and $t_{41} = 0.1$ ns, respectively, which are reduced to allow for simulation within the computational window (<3 ps) in the time-domain approach (Supplementary Figs. 13–15). **d**, Simulated input–output curve showing a threshold-like power dependence with laser thresholds comparable to the experimental values. **e**, Simulated time-dependent evolution of population density describing upconverting nanolasing and the associated population inversion above threshold at 27 kW cm^{-2} (marked star position in **d**). Plots of N_1 and N_5 curves stayed at almost zero since the population decayed quickly to N_0 and N_4, respectively.

Online content

Any methods, additional references, Nature Research reporting summaries, source data, statements of code and data availability and associated accession codes are available at https://doi.org/10.1038/s41563-019-0482-5.

Received: 23 March 2019; Accepted: 13 August 2019;
Published online: 23 September 2019

References

1. Hill, M. T. & Gather, M. C. Advances in small lasers. *Nat. Photon.* **8**, 908–918 (2014).
2. Ma, R. M. & Oulton, R. F. Applications of nanolasers. *Nat. Nanotechnol.* **14**, 12–22 (2019).
3. Wang, D., Wang, W., Knudson, M. P., Schatz, G. C. & Odom, T. W. Structural engineering in plasmon nanolasers. *Chem. Rev.* **118**, 2865–2881 (2017).
4. Fan, F. J. et al. Continuous-wave lasing in colloidal quantum dot solids enabled by facet-selective epitaxy. *Nature* **544**, 75–79 (2017).
5. Tamboli, A. C. et al. Room-temperature continuous-wave lasing in GaN/InGaN microdisks. *Nat. Photon.* **1**, 61–64 (2007).
6. Wang, D. et al. Band-edge engineering for controlled multi-modal nanolasing in plasmonic superlattices. *Nat. Nanotechnol.* **12**, 889–894 (2017).
7. Zhou, W. et al. Lasing action in strongly coupled plasmonic nanocavity arrays. *Nat. Nanotechnol.* **8**, 506–511 (2013).
8. Oulton, R. F. et al. Plasmon lasers at deep subwavelength scale. *Nature* **461**, 629–632 (2009).
9. Lu, Y. J. et al. Plasmonic nanolaser using epitaxially grown silver film. *Science* **337**, 450–453 (2012).
10. Zhu, H. et al. Lead halide perovskite nanowire lasers with low lasing thresholds and high quality factors. *Nat. Mater.* **14**, 636–642 (2015).
11. Huang, M. H. et al. Room-temperature ultraviolet nanowire nanolasers. *Science* **292**, 1897–1899 (2001).
12. Wang, S. et al. Unusual scaling laws for plasmonic nanolasers beyond the diffraction limit. *Nat. Commun.* **8**, 1889 (2017).
13. Hakala, T. K. et al. Lasing in dark and bright modes of a finite-sized plasmonic lattice. *Nat. Commun.* **8**, 13687 (2017).
14. Sidiropoulos, T. P. H. et al. Ultrafast plasmonic nanowire lasers near the surface plasmon frequency. *Nat. Phys.* **10**, 870–876 (2014).
15. Zhang, Q. et al. A room temperature low-threshold ultraviolet plasmonic nanolaser. *Nat. Commun.* **5**, 4953 (2014).
16. Zhou, B., Shi, B., Jin, D. & Liu, X. Controlling upconversion nanocrystals for emerging applications. *Nat. Nanotechnol* **10**, 924–936 (2015).
17. Gargas, D. J. et al. Engineering bright sub-10-nm upconverting nanocrystals for single-molecule imaging. *Nat. Nanotechnol.* **9**, 300–305 (2014).
18. Wu, S. et al. Non-blinking and photostable upconverted luminescence from single lanthanide-doped nanocrystals. *Proc. Natl Acad. Sci. USA* **106**, 10917–10921 (2009).
19. Anderson, R. B., Smith, S. J., May, P. S. & Berry, M. T. Revisiting the NIR-to-visible upconversion mechanism in β-NaYF4:Yb3+,Er3+. *J. Phys. Chem. Lett.* **5**, 36–42 (2014).
20. Zhu, H. et al. Amplified spontaneous emission and lasing from lanthanide-doped up-conversion nanocrystals. *ACS Nano.* **7**, 11420–11426 (2013).
21. Fernandez-Bravo, A. et al. Continuous-wave upconverting nanoparticle microlasers. *Nat. Nanotechnol.* **13**, 572–577 (2018).
22. Haider, G. et al. A highly-efficient single segment white random laser. *ACS Nano.* **12**, 11847–11859 (2018).
23. Ostrowski, A. D. et al. Controlled synthesis and single-particle imaging of bright, sub-10 nm lanthanide-doped upconverting nanocrystals. *ACS Nano.* **6**, 2686–2692 (2012).
24. Tian, B. et al. Low irradiance multiphoton imaging with alloyed lanthanide nanocrystals. *Nat. Commun.* **9**, 3082 (2018).
25. Schuck, P. J., Willets, K. A., Fromm, D. P., Twieg, R. J. & Moerner, W. E. A novel fluorophore for two-photon-excited single-molecule fluorescence. *Chem. Phys.* **318**, 7–11 (2005).
26. Grim, J. Q. et al. Continuous-wave biexciton lasing at room temperature using solution-processed quantum wells. *Nat. Nanotechnol.* **9**, 891–895 (2014).
27. Samuel, I. D. & Turnbull, G. A. Organic semiconductor lasers. *Chem. Rev.* **107**, 1272–1295 (2007).
28. Nielsen, M. P., Shi, X. Y., Dichtl, P., Maier, S. A. & Oulton, R. F. Giant nonlinear response at a plasmonic nanofocus drives efficient four-wave mixing. *Science* **358**, 1179–1181 (2017).
29. Yuan, P. et al. Plasmon enhanced upconversion luminescence of NaYF4:Yb,Er@SiO2@Ag core–shell nanocomposites for cell imaging. *Nanoscale* **4**, 5132–5137 (2012).

30. Sun, Q. C. et al. Plasmon-enhanced energy transfer for improved upconversion of infrared radiation in doped-lanthanide nanocrystals. *Nano Lett.* **14**, 101–106 (2014).
31. Auguie, B. & Barnes, W. L. Collective resonances in gold nanoparticle arrays. *Phys. Rev. Lett.* **101**, 143902 (2008).
32. Zou, S., Janel, N. & Schatz, G. C. Silver nanoparticle array structures that produce remarkably narrow plasmon lineshapes. *J. Chem. Phys.* **120**, 10871–10875 (2004).
33. Yang, A. et al. Real-time tunable lasing from plasmonic nanocavity arrays. *Nat. Commun.* **6**, 6939 (2015).
34. Wang, D. Q. et al. Stretchable nanolasing from hybrid quadrupole plasmons. *Nano Lett.* **18**, 4549–4555 (2018).
35. Liu, Q. et al. Single upconversion nanoparticle imaging at sub-10 W cm^{-2} irradiance. *Nat. Photon.* **12**, 548–553 (2018).
36. Liu, Y. et al. Amplified stimulated emission in upconversion nanoparticles for super-resolution nanoscopy. *Nature* **543**, 229–233 (2017).
37. Wei, W. et al. Cross relaxation induced pure red upconversion in activator- and sensitizer-rich lanthanide nanoparticles. *Chem. Mater.* **26**, 5183–5186 (2014).
38. Tajon, C. A. et al. Photostable and efficient upconverting nanocrystal-based chemical sensors. *Opt. Mater.* **84**, 345–353 (2018).
39. Ma, R. M., Oulton, R. F., Sorger, V. J., Bartal, G. & Zhang, X. Room-temperature sub-diffraction-limited plasmon laser by total internal reflection. *Nat. Mater.* **10**, 110–113 (2011).
40. Teitelboim, A. et al. Energy transfer networks within upconverting nanoparticles are complex systems with collective, robust, and history-dependent dynamics. *J. Phys. Chem. C.* **123**, 2678–2689 (2019).
41. Chen, S. et al. Near-infrared deep brain stimulation via upconversion nanoparticle-mediated optogenetics. *Science* **359**, 679–684 (2018).

Acknowledgements

This work was supported by the National Science Foundation (NSF) under DMR-1608258 and the Vannevar Bush Faculty Fellowship from DOD under N00014-17-1-3023. The work at the Molecular Foundry was supported by the Office of Science, Office of Basic Energy Sciences, of the US Department of Energy under contract no. DE-AC02-05CH11231. Portions of this research were supported by the Global Research Laboratory Program through the National Research Foundation of Korea funded by the Ministry of Science and ICT (grant no. 2016911815). The work used the Northwestern University Micro/Nano Fabrication Facility, which is partially supported by Soft and Hybrid Nanotechnology Experimental Resource (grant no. NSF ECCS-1542205), the Materials Research Science and Engineering Center (grant no. DMR-1720139), and the State of Illinois and Northwestern University. A.T. was supported by the Weizmann Institute of Science—National Postdoctoral Award Program for Advancing Women in Science. We thank F. Scotognello for assistance with the ultrafast lasing measurements at the Molecular Foundry.

Author contributions

A.F.-B. and D.W. contributed equally to this work. A.F.-B. measured non-linear optical properties, lasing emissions and coherence characteristics of upconverting nanoparticles and nanolasers. D.W. and J.G. fabricated plasmonic nanoparticle arrays. D.W. characterized the linear optical properties and modelled plasmon resonances and upconverting lasing. E.S.B. contributed to data analysis. A.F.-T. and A.B. performed $g^{(2)}$ measurements. C.T., E.M.C. and B.E.C. contributed to upconverting nanoparticle synthesis. All authors analysed the data, wrote and revised the manuscript.

Competing interests

The authors declare no competing interests.

Additional information

Supplementary information is available for this paper at https://doi.org/10.1038/s41563-019-0482-5.

Correspondence and requests for materials should be addressed to P.J.S. or T.W.O.

Reprints and permissions information is available at www.nature.com/reprints.

Publisher's note Springer Nature remains neutral with regard to jurisdictional claims in published maps and institutional affiliations.

Methods

Synthesis of core–shell UCNPs. We synthesized lanthanide-doped UCNP cores of beta phase NaYF4 (β-$NaYF_4$) with doping concentrations of 20% Yb^{3+}, 20% Er^{3+} and 20% Gd^{3+}, similar to methods previously described[24,38]. The precursors were: $YbCl_3 \cdot H_2O$ (0.080 mmol, 32 mg), YCl_3 (0.16 mmol, 31 mg), $ErCl_3$ (0.08 mmol, 22 mg), $GdCl_3$ (0.080 mmol, 21 mg), oleic acid (3.25 g) and 1-octadecene (ODE, 4 ml), which we stirred together—purging with N_2 every 15 min for 1 h—while heating at 110 °C under vacuum in a three-necked flask that included an in-reaction thermocouple. The dissolved lanthanide solution was cooled in an N_2 atmosphere, followed by the addition of NH_4F (2.0 mmol, 74 mg), ODE (3 ml) and sodium oleate (1.25 mmol, 382 mg) to the flask. Next, we stirred the mixture for 30 min under vacuum at room temperature, and then heated it for 45 min at 317 °C. After heating, the reaction flask was cooled to 40 °C using a strong stream of air. The product was transferred to a 50-ml centrifuge tube, where 10 ml of ethanol added. The tube was centrifuged for 3 min at an acceleration of 3,000*g*. The supernatant was then decanted and 3 ml of hexane, which was used to wash the reaction flask, was added to the pellet. Sonication was then used to disperse the pellet. Following this dispersion, the tube was then centrifuged again for 3 min at 3,000*g*. We transferred the supernatant to a new tube, added 5 ml of ethanol and centrifuged the tube again at 3,000*g* for 3 min. The pellet was dispersed in 1 ml of hexane and precipitated with ethanol (5 ml) two additional times. Finally, we dispersed the resulting pellet in 15 ml of anhydrous hexane.

A layer-by-layer protocol that incorporated 20% Gd^{3+} to facilitate the growth of β-phase morphology[42] was used to overgrow inert 2-nm $NaYF_4$ shells on these 10-nm cores. We added a 28 nmol hexane dispersion of core UCNPs to a 50-ml three-neck flask, then evaporated the hexane under N_2. After adding 6 ml of ODE and 4 ml of oleic acid, the flask was stirred under vacuum for 1 h at 70 °C. Ln oleates were prepared by heating at 110 °C YCl_3 (0.40 mmol, 78 mg), $GdCl_3$ (0.10 mmol, 26 mg), oleic acid (2 ml) and 1-ODE (3 ml) under vacuum for 1 h. In a separate flask, we dissolved sodium trifluoroacetate (1.20 mmol, 16 mg) in oleic acid (3 ml) and stirred for 1 h under vacuum at room temperature. The flask with UCNPs was purged with N_2 and heated for 10 min at 280 °C to allow temperature stabilization. As in previous work[38], we injected the shell precursors using sequential injections of Ln and Na/F precursors every 15 min. The reaction was stirred for an additional 30 min at 280 °C after four rounds of injections and then a strong air stream was used to cool the flask. Using the same protocol for core UCNPs, we then isolated and stored the core–shell UCNPs. Using TEM characterization, we measured core–shell UCNPs with final diameters of 13.9 ± 0.8 nm (Supplementary Fig 1).

Nanoparticle characterization. We diluted stock solutions of oleate-capped UCNPs 100-fold in hexane for TEM imaging. Here, we adsorbed 10 µl onto a carbon film/holey carbon on a 400-mesh copper grid (Ted Pella). We wicked excess hexane from the grid and allowed it to dry in the hood. Using a FEI Tecnai TEM or Philips CM200/FEG, standard TEM images were collected in scanning electron microscopy mode and sizing statistics were gathered using ImageJ software on approximately 100 nanoparticle images. To acquire incoherent *Z*-contrast images, we used a primary beam energy of 300 keV and a high angle annular dark field detector (Fischione) on the TEAM I aberration-corrected electron microscope (Thermo Fischer Scientific) in scanning transmission mode. For the core–shell nanoparticles, core–shell structures are apparent based on the *Z*-contrast with a sharp change in the intensity of the atomic columns that corresponds to differences in Ln^{3+} content between core and shell. UCNP cores do not show this transition.

Preparation of plasmonic nanopillar arrays. Arrays of Ag nanopillars with a cylindrical shape (diameter 80 nm, height 50 nm) were fabricated with a large-scale nanofabrication process referred to as PEEL[43] (photolithography, Si etching, metal deposition and metal film lift-off). First, phase-shifting photolithography with a poly(dimethylsiloxane) mask generated periodic photoresist posts on Si wafers. The patterns were then transferred into free-standing Au nanohole films by PEEL. Finally, we created Ag nanopillar arrays by metal deposition through the nanohole-array mask on fused silica and removed the mask with Scotch tape. A 2-nm Cr layer in-between facilitated better adhesion between Ag nanopillars and the substrate. To protect the Ag nanopillars from deleterious oxidation effects, we used atomic layer deposition to form a 5-nm Al_2O_3 layer around the nanopillar surface.

Preparation of lanthanide-based nanoparticles plasmon nanolasers. Solution-processed UCNPs were drop-cast on top of Ag nanopillar arrays (diameter $d = 80$ nm, height $h = 50$ nm). The thickness of the coating can be controlled with the concentration of the nanocrystals in solution. The drop-cast film thickness was around 150 nm for the devices discussed here. The measured transmission spectra suggested that sharp lattice plasmon resonances were preserved after coating Ag nanopillars with Yb^{3+}/Er^{3+} UCNP emitters.

Confocal microscopy and spectroscopy. For direct UCNP excitation, a dispersion of nanoparticles was added to a glass coverslip and placed on an inverted confocal microscope (Nikon). A 980-nm laser (ThorLabs) was directed into the back aperture of a 0.1 numerical aperture ×4 objective (Nikon), and focused directly on the sample. The emitted light was collected back through the same objective, filtered by one 496-nm long-pass and one 745-nm short-pass filter (Semrock, Inc., Brightline multiphoton filter), in addition to a 720SP dichroic and sent to an LN_2-cooled charge-coupled device-equipped spectrometer (Princeton Instruments). The same confocal microscope was used for excitation of the upconverting plasmon nanolaser and spectroscopy studies of laser modes. Different gratings are available in the dispersion system, namely 150 grooves per mm and 600 grooves per mm, providing different spectral resolution and dynamic ranges. The resolution of the spectrometer is 0.1 nm, which could be improved slightly by closing the slit of the spectrometer at a cost of collection efficiency. For power dependence measurements for the evaluation of lasing action, a neutral density wheel with a continuously variable density was used, synchronized with the collection system and automatically rotated by an Arduino-controlled rotator. Powers were simultaneously recorded by a Thorlabs power meter by using a glass coverslip to reflect ~10% of the incoming flux. The powers were in-line recorded in H5-files as metadata for each independent file.

Wide-field imaging. For wide-field imaging, a complementary metal-oxide-semiconductor Andor Neo 5.5 camera was attached to the microscope without going through the confocal optical pathway. Instead, the signal was collected laterally on one of the external side ports of the microscope.

Photon statistics. A second-order correlation measurement was implemented using a Hanbury-Brown and Twiss setup with a 50/50 beam splitter and 2 MPD detectors. The $g^{(2)}$ optical second-order cross correlation is defined as:

$$g^{(2)}(\tau) = \langle I_{\mathrm{det1}}(t) \times I_{\mathrm{det2}}(t+\tau) \rangle$$

where $I_{\mathrm{det1}}(t)$ and $I_{\mathrm{det2}}(t)$ are the signal intensities measured at the two detectors (the two discrete photon streams collected by the two channels). The brackets denote the expectation value and t and τ are the photon arrival time and delay. The counts in the $g^{(2)}$ histogram are the number of photon pairs detected for different delays using the two detectors (which means it should vary with the measurement length, selected bin size and signal intensity). The normalized $g^{(2)}$ is:

$$g^{(2)} = \frac{\langle I_{\mathrm{det1}}(t) \times I_{\mathrm{det2}}(t+\tau) \rangle}{(\langle I_{\mathrm{det1}}(t) \rangle \times \langle I_{\mathrm{det2}}(t+\tau) \rangle)}$$

which is the normalization by division of the mean signal of the two detectors.

The second-order correlation has been used to evaluate the photon statistics for the upconverting plasmon nanocavity array, producing upconverted lasing by coupling these nanocavity arrays with Yb^{3+} and Er^{3+} ions doped in a $NaYF_4$ matrix, which are able to upconvert NIR 980 nm excitation wavelength to red (around 660) nm visible emission from the Er. The emission at around 660 nm coupled resonantly with the engineered plasmon nanocavity array, and when the excitation power was above the threshold, lasing appeared selected from Er^{3+} emission at around 660 nm. The emission spectra show that the nanocavity mode modifies the Er^{3+} spontaneous emission even at low pump powers, funnelling energy into the preferential mode, which increases in intensity and narrows with increased pump power. The plot of emission intensity versus pump power shows that its intensity and linewidth are power dependent with a $P_{\mathrm{th}} \sim 30$–$70\ \mathrm{W\,cm^{-2}}$ for CW pumping and $P_{\mathrm{th}} \sim 32$–$300\ \mathrm{W\,cm^{-2}}$ average power for pulsed pumping conditions.

The plasmon lasers were measured at above-threshold excitation pump powers of $112\ \mathrm{W\,cm^{-2}}$ for CW and $230\ \mathrm{W\,cm^{-2}}$ for pulsed pumping at 980 nm. Supplementary Fig. 10 depicts the $g^{(2)}$ histogram for the upconverted lasing at around 660 nm for above-threshold powers (CW and pulsed pumping schemes), showing that the normalized $g^{(2)}$ function is one for both pumping schemes. This demonstrates that there is no temporal correlation between the emitted photons, which is a signature of CW lasing. Below- and above-threshold measurements of the laser emission yield a small photon bunching for below laser thresholds at $g^{(2)}(t=0)$ attributed to amplified spontaneous emission; a comparison to Er^{3+} spontaneous emission is added to the plot in Supplementary Fig. 11. As a reference, the second-order optical cross correlation $g^{(2)}$ of the 80 MHz chameleon laser at 800 nm was measured with the same detector configuration. Supplementary Fig. 12 depicts the $g^{(2)}$ histogram of the chameleon laser at 800 nm, showing the pulsing of the 80 MHz laser with bunching peaks rising every 12.5 ns corresponding to the laser repetition rate (bunching peaks every 12.5 ns corresponds to the laser pulse train). Note that there is no bunching peak recorded for the upconverting plasmon nanocavity laser, which instead shows photon statistics typical of CW lasing emission. A Poissonian distribution is not sufficient to indicate CW lasing behaviour, since lanthanide spontaneous emission also exhibits this. However, the highly non-linear scaling with power shows slopes as high as ten, which agrees with our upconverting lasing modelling, and the simultaneous mode narrowing experienced at threshold powers indicates lasing behaviour that happens in a CW fashion.

Finite-difference time-domain (FDTD) simulations. FDTD calculations with commercial software (FDTD solution, Lumerical Inc.) were used to model the linear optical responses of Ag nanopillar arrays. The optical constant of Ag was taken from Johnson and Christy measurements (wavelength, 400–1,000 nm). A uniform mesh size of 4 nm (x, y and z) was used to ensure the accuracy of optical field calculations within the Ag nanopillars.

Simulation of upconverting nanolasing was performed by home-built MATLAB codes, where a six-level one-electron model was integrated for modelling Yb^{3+}/Er^{3+}-co-doped UCNPs. The narrow lattice plasmon resonance provides selective enhancement only for the Er^{3+} red emission without directly affecting other energy transfer processes and, hence, we could use a simplified six-level model to approximately describe the upconverting lasing process (Supplementary Figs. 13–15). In the semiquantum system, we set the cylindrical Ag nanopillar size $d = 80$ nm and height $h = 50$ nm, pump wavelength at $\lambda_a = 980$ nm, emission at $\lambda_e = 660$ nm and index $n = 1.42$, close to experimental conditions. The decay lifetimes were $t_{54} = t_{10} = 10$ fs, $t_{41} = 0.1$ ns and $t_{50} = t_{32} = t_{30} = 1$ ns. We initially pumped the six-level system from the ground state (population density $N_0 = 1$, $N_1 = N_2 = N_3 = N_4 = N_5 = 0$) and collected all emitted flux with a plane monitor 0.3 μm away from the nanopillars. Er^{3+} emitter concentration was $C = 3$ mM. The whole simulation window was within ~1 ps, and time-dependent evolution of population density at different energy levels was tracked to probe the characteristic population inversion for lasing action.

Reporting Summary. Further information on research design is available in the Nature Research Reporting Summary linked to this article.

Data availability

The data that support the findings of this study are available from the corresponding authors on reasonable request.

Code availability

The codes used for this study are available from the corresponding authors on reasonable request.

References

42. Levy, E. S. et al. Energy-looping nanoparticles: harnessing excited-state absorption for deep-tissue imaging. *ACS Nano.* **10**, 8423–8433 (2016).
43. Henzie, J., Lee, M. H. & Odom, T. W . Multiscale patterning of plasmonic metamaterials. *Nat. Nanotechnol.* **2**, 549–554 (2007).

nature research

Corresponding author(s): Teri W. Odom; P. James Schuck

Lasing Reporting Summary

Nature Research wishes to improve the reproducibility of the work that we publish. This form is intended for publication with all accepted papers reporting claims of lasing and provides structure for consistency and transparency in reporting. Some list items might not apply to an individual manuscript, but all fields must be completed for clarity.

For further information on Nature Research policies, including our data availability policy, see Authors & Referees.

Experimental design

Please check: are the following details reported in the manuscript?

1. Threshold

Plots of device output power versus pump power over a wide range of values indicating a clear threshold	☒ Yes ☐ No	• We plotted input-output curves over a wide range in log-log scale (Figures 1e-f, Figure 3b). • A clear lasing threshold was shown in the experiments (29, 32, 70, 210, and 300 W/cm2), where significant changes in slope are evident.

2. Linewidth narrowing

Plots of spectral power density for the emission at pump powers below, around, and above the lasing threshold, indicating a clear linewidth narrowing at threshold	☒ Yes ☐ No	• The emission spectra were plotted below, near, and above the threshold (Figures 1e-f, Figure 3b). • The linewidth of emission spectra decreased from ~2 nm (below threshold) to <1 nm (above threshold) as lasing happened, and the narrowing correlates directly with the slope changes in the input-output curves (Figure 1f).
Resolution of the spectrometer used to make spectral measurements	☒ Yes ☐ No	• The resolution of the spectrometer (LN2-cooled CCD-equipped spectrometer, Princeton Instruments) is 0.1 nm (Methods).

3. Coherent emission

Measurements of the coherence and/or polarization of the emission	☒ Yes ☐ No	• The single emission beam exhibited only minor beam divergence in the far-field (Figure 2b; divergence ca. 0.5°). • The emission beam shows the polarized character of the pump source (Figures 2c, d). • Output lasing showed extremely narrow spectral linewidth (< 1 nm), close to the resolution of the spectrometer. • Temporal coherence characterization by g(2) measurement demonstrates that the upconverting nanolaser can achieve CW emission under both CW and pulsed pump conditions (Figures S10-12).

4. Beam spatial profile

Image and/or measurement of the spatial shape and profile of the emission, showing a well-defined beam above threshold	☒ Yes ☐ No	• Far-field emission pattern of upconverting nanolasing was analyzed by a high-resolution CCD beam profiler. • The single emission beam exhibited only minor beam divergence in the far-field (ca. 0.5°, Figures 2a-b).

5. Operating conditions

Description of the laser and pumping conditions *Continuous-wave, pulsed, temperature of operation*	☒ Yes ☐ No	• We stated clearly the pumping conditions in both the text and in Methods (a 980-nm laser diode, ThorLabs, for CW; and Ti-sapphire laser at 980-nm for pulsed excitation).
Threshold values provided as density values (e.g. W cm^{-2} or J cm^{-2}) taking into account the area of the device	☒ Yes ☐ No	• Pump power values were all provided in W/cm2 units (e. g. threshold 70 W/cm2).

6. Alternative explanations

Reasoning as to why alternative explanations have been ruled out as responsible for the emission characteristics *e.g. amplified spontaneous, directional scattering; modification of fluorescence spectrum by the cavity*	☒ Yes ☐ No	• Shifting the cavity resonance from 650 nm (a0 = 450 nm) to 660 nm (a0 = 460 nm) induced evident change of lasing wavelength, which demonstrated that single-mode upconverting lasing is directly determined by the plasmonic nanocavities (Figures 3a-b). • Above lasing threshold, we observed a significant increase in exponential growth slope (s = 4.4; Figure 1f) in the input-output curve, compared to the maximum slope observed for spontaneous emission in this nonlinear medium (s = 2.2; Figure S4).

7. Theoretical analysis

Theoretical analysis that ensures that the experimental values measured are realistic and reasonable *e.g. laser threshold, linewidth, cavity gain-loss, efficiency*	☒ Yes ☐ No	• We used a semi-quantum model and a time-domain approach to model the upconverting nanolasing, and captured characteristic population inversion and strong optical nonlinearities (Figures 3c-e, Figures S13-15). • The calculated lasing threshold occurred at an average power of 270 W/cm2 (Figure 3d), comparable with experiments.

8. Statistics

Number of devices fabricated and tested	☒ Yes ☐ No	• We characterized 7 lasing devices with no apparent degradation to date.
Statistical analysis of the device performance and lifetime (time to failure)	☒ Yes ☐ No	• Over more than 6 hours under continuous irradiation, we did not observe any optical or thermal damage; the mode intensity remained constant, and only minimal shifts in mode frequency (< 0.15 nm) occurred (Figure 2f). • Ag nanopillar samples (protected with a 5-nm Al2O3 layer by atomic layer deposition) maintain integrity for years.